Engineering Failure Analysis 115 (2020) 104638

Contents lists available at ScienceDirect

Engineering Failure Analysis

journal homepage: www.elsevier.com/locate/engfailanal

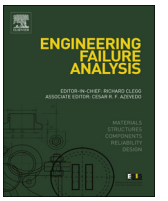

Field and numerical investigations on the lower coal seam entry failure analysis under the remnant pillar

Zizheng Zhang[a,*], Min Deng[b], Xiangyu Wang[c], Weijian Yu[b], Fei Zhang[d], Viet Doan Dao[e]

[a] Work Safety Key Lab on Prevention and Control of Gas and Roof Disasters for Southern Goal Mines, Hunan Provincial Key Laboratory of Safe Mining Techniques of Coal Mines, Hunan University of Science and Technology, Xiangtan, Hunan 411201, China
[b] School of Resource & Environment and Safety Engineering, Hunan University of Science and Technology, Xiangtan, Hunan 411201, China
[c] School of Mining, China University of Mining and Technology, Xuzhou, Jiangsu 221116, China
[d] China Coal Technology Engineering Group Chongqing Research Institute, Chongqing, China
[e] Hanoi University of Mining and Geology, Hanoi 100803, Viet Nam

ARTICLE INFO

Keywords:
Multi-seam mining
Numerical simulation
Severe deformation
Failure mechanism
Lower coal seam entry

ABSTRACT

Extraction of multiple seam using fully mechanized coal mining technology caused severe deformations in the lower coal seam roadways in Zhaiyadi Coal Mine in Shanxi Province, China. Understanding the characteristics of the lower coal seam entry failure mechanism under the remnant pillar is the first step in determining a reasonable location of the lower coal seam entry. Characteristics of the lower coal seam entry failure mechanism under the remnant pillar are investigated by means of numerical simulations and in-situ observations. To improve the reliability of the numerical simulations, the global model is validated by comparing the surrounding rock deformation of 3905 headgate with the in-situ observation data due to the extraction of Panel 3805. The numerical simulation results of the global model indicate that the original 3905 headgate under the remnant coal pillar is located in the vertical stress concentration zone and horizontal stress concentration zone. Firstly, the peak vertical stress concentration factor in the coal seam 9# (the lower coal seam) is 4.9, located 100 m behind the active Panel 3805 while the peak horizontal stress concentration factor in the coal seam 9# is 2.1, and located 30 m behind the active Panel 3805. When the delay distance to the active Panel 3805 is 80 m, the stress transmission angle reaches a constant value of 30.9°. Secondly, both the ratio of coal pillar rib deformation to solid coal rib and the ratio of roof subsidence to floor heave increase as the delay distance to the active Panel 3805 increases. Finally, numerical results show that the designed 3905 headgate located 25 m to 30 m away from the middle of the remnant coal pillar would be an alternative scheme, located out of the floor horizontal stress concentration and vertical stress concentration in the coal seam 9#. The findings in this study will help to provide a basis to select a reasonable location for lower coal seam roadways under similar mining and geological conditions.

* Corresponding author at: Work Safety Key Lab on Prevention and Control of Gas and Roof Disasters for Southern Goal Mines, Hunan Provincial Key Laboratory of Safe Mining Techniques of Coal Mines, Hunan University of Science and Technology, China.
E-mail address: 1010096@hnust.edu.cn (Z. Zhang).

https://doi.org/10.1016/j.engfailanal.2020.104638
Received 9 March 2020; Received in revised form 26 May 2020; Accepted 26 May 2020
Available online 28 May 2020
1350-6307/

1. Introduction

Multi-seam longwall coal mining has been widely used in China and other countries [1–5]. Undermining and overmining are the two most common types of mining methods for multi-seam longwall coal mining. In China, the previous study focused on qualitative summary with lack of the quantitative suggestions, especially the entry layout of the lower coal seam. However, the upper coal seam extraction involves many challenges such as the stress concentrations caused by the remnant pillars of the upper coal seam, entry stability control of the lower coal seam, rock burst and determining reasonable longwall panel and entry layouts for the lower coal seam [6–11]. As for undermining, the concentrated residual stress of the remnant pillar and gob boundary is transferred to the floor after mining the upper coal seam [12,13]. The floor stress distribution characteristics would change due to the remnant pillar. As a result, a stress concentrated zone would generate and develop. The entry located in or beside the stress concentrated zone would be difficult to maintain during the mining process of the upper coal seam [14,15]. Therefore, evaluating the influence of the remnant pillars of the upper coal seam and the upper coal seam mining on the roadway stability of the lower coal seam is of great importance, especially for undermining.

Research on floor stress distribution due to the remnant pillars and the gob boundary of the upper coal seam were carried out by theoretical calculation and numerical simulation. Pressure bulb theory and pressure arching theory were both used to assume the load transfer characteristics of the remnant pillar [16–18]. Haycocks studied the pressure bulb concept through the photoelastic models [16]. Peng developed a simplified model representing pressure interaction between columnized pillars by the tributary area method [17]. Haycocks investigated the pressure arching effect in multiple-seam by finite-element and stress vector plots [18]. In China, Yan [19], Liu [20], and Yang [21] studied the floor stress distribution after the two adjacent longwall panels had been mined out by using semi-infinite plane theory. Meng studied the floor stress distribution based on an elastic mechanical model and abutment pressure distribution in front of the longwall panel of the overlying coal seam [22]. Zhu studied the stress distribution of the relatively fixed position on the floor based on the floor stress mathematical model and elasticity theory [23]. The aforementioned theoretical studies of floor stress distribution were mainly based on the elastic mechanical model. Zhang studied the vertical and lateral stress in the floor rock interlayer after protective seam exploitation through FLAC3D [14]. Wang studied the surrounding rock deformation of the roadway with different layer spacing and inner stagger distance is also studied through FLAC3D [24]. Liu analyzed the stress distribution of lower seams with three kinds of longwall panels by using UDEC [25]. Xiao conducted the vertical stress, horizontal stress, and stress difference distribution characteristics by using UDEC [26]. All of the research results indicate the importance of remnant pillar width and interburden parameters (thickness and strength) in affecting the floor stress distribution as well as the entry layout of the underlying coal seam.

It should be pointed out that the floor stress distribution presents an extended state with a common stress transmission angle. Particularly, the influence depth of abutment pressure in the remnant pillar of the upper coal seam is closely associated with the remnant pillar width of the upper coal seam. Xiao [26], Zhang [27], and Kong [28] conducted the depth of the destroyed floor through the slip line theory. Tan carried out in-situ investigations of the failure evolution of overlying strata induced by the mining of multi-seam in the Gaojialiang and Jinhuagong mines, China [3]. Suchowerska evaluated the vertical stress and horizontal stress changes in multi-seam mining under supercritical longwall panels [10,29]. The stress distribution of the lower coal seam varies concerning the remnant coal pillar of the upper coal seam. The ground control of the underground entries in the lower coal seam is closely related to the location of the roadways, especially under the remaining coal pillar of the upper coal seam. The large deformation of the lower coal seam entries significantly influenced mining and excavation safety. Special attention should be paid to the ground control problems induced by the extraction of the upper coal seam.

At present, the panel 3805 in Zhaiyadi Coal Mine is mined out with the remnant coal pillar 30 m wide. The original 3905 headgate is located under the remnant pillar. In-situ observation results during the 3905 headgate was excavated show that the deformation of 3905 headgate increases intensively and is severe, which involves 3905 headgate stability control challenges. Therefore, it is beneficial to find the reason for the severe deformation of 3905 headgate and select a reasonable position of the lower coal seam entry.

In the present work, a case study in the Zhaiyadi Coal Mine was analyzed to reveal the lower coal seam entry failure mechanism under the remnant pillar based on the in-situ observations and numerical simulations. It is hoped that this engineering failure analysis case can offer an insight into the lower coal seam entry failure mechanism under the remnant pillar and help to select a reasonable position of the lower coal seam entry under the similar engineering and geological condition.

2. Engineering overview

2.1. Description of the mine study site

The Zhaiyadi Coal Mine is located in Lvliang City, Shanxi Province, China. Currently, coal seam 8# (average thickness 3.0 m) and coal seam 9# (average thickness 4.5 m) are being extracted using fully mechanized coal mining technology. Three-entry systems were used in the longwall panel layout in coal seams 8# and 9#. Barrier pillars 30 m wide were designed both in the longwall panel of coal seams 8# and 9#. The longwall Panel 3805 with 3.0 m mechanized mining height was composed of three entries 3.2 m high by 4.8 m wide. The longwall Panel 3905 with 4.5 m mechanized mining height was composed of three entries 3.6 m high and 4.8 m wide. The average overburden depth of coal seam 9# was 415 m. The coal seams 8# and 9# were dipped with an average of 2°, 5°, respectively. The average interburden thickness (IT) between coal seam 8# and coal seam 9# was 14.0 m. Panel 3805 and panel 3905 were both 200 m wide. A schematic diagram of the longwall panel layout and a simplified geological column are provided in Fig. 1.

In practice, 3905 headgate was excavated when Panel 3805 was mined. The excavating direction (ED) of 3905 headgate was

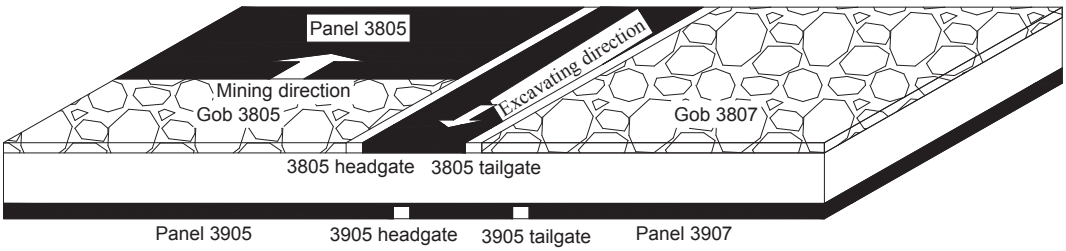

(a)

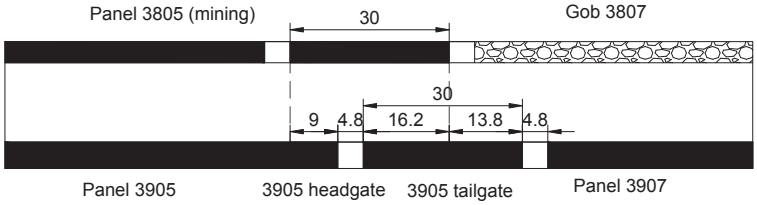

(b)

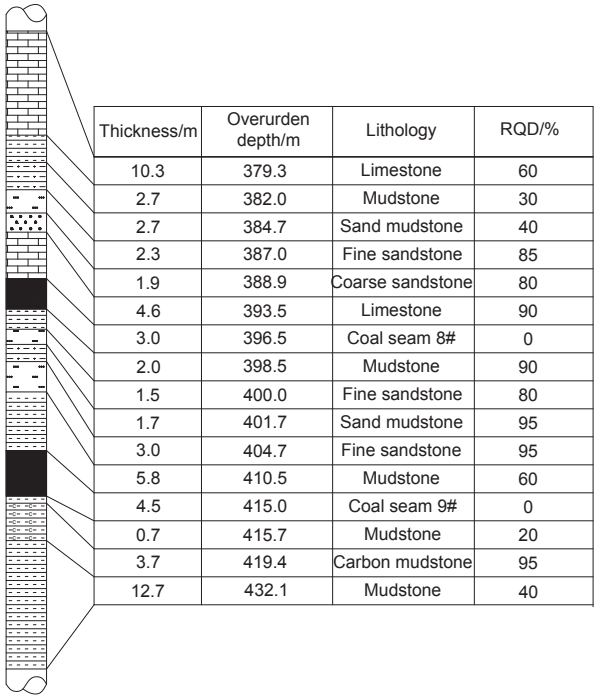

Thickness/m	Overurden depth/m	Lithology	RQD/%
10.3	379.3	Limestone	60
2.7	382.0	Mudstone	30
2.7	384.7	Sand mudstone	40
2.3	387.0	Fine sandstone	85
1.9	388.9	Coarse sandstone	80
4.6	393.5	Limestone	90
3.0	396.5	Coal seam 8#	0
2.0	398.5	Mudstone	90
1.5	400.0	Fine sandstone	80
1.7	401.7	Sand mudstone	95
3.0	404.7	Fine sandstone	95
5.8	410.5	Mudstone	60
4.5	415.0	Coal seam 9#	0
0.7	415.7	Mudstone	20
3.7	419.4	Carbon mudstone	95
12.7	432.1	Mudstone	40

(c)

Fig. 1. Schematic diagram of the multi-seam mining layout and geological column settings. (a) Schematic diagram of the multi-seam mining layout; (b) Plan view of the multi-seam mining layout (unit:m); (c) Geological column settings.

exactly opposite with the mining direction (MD) of Panel 3805 (see Fig. 1b). The 3905 headgate was primarily supported with rockbolts and anchor cables and reinforced by secondary supports with hydraulic props. High-strength rockbolts 22 mm in diameter and 2400 mm long were used in the roof support and the coal-ribs support. The rockbolts of every row were spaced at 800 mm both in the roof and coal rib, and the rows were located at 800 mm intervals along the length of 3905 headgate of both the roof and the coal rib. A row of anchor cables, each 17.8 mm in diameter and 8000 mm long, were also used in the roof support. The anchor cables of every row were placed 1600 mm apart, and the rows were spaced 2400 mm apart along the length of 3905 headgate.

2.2. In-situ observation of the surrounding rock deformation in the 3905 headgate

The 3905 headgate was located under the remnant pillar of coal seam 8#. The 3905 headgate would be subjected to the mining

Fig. 2. Deformation characteristics of 3905 headgate due to retreating Panel 3805.

effects of the Panel 3805 and the stress concentration effects of the remnant pillar for coal seam 8#. Fig. 2 shows the severely deformed 3905 headgate behind the active Panel 3805. The positive distance to the active Panel 3805 means that the position is located at front of the active Panel 3805. Meanwhile, the negative distance to the active Panel 3805 means that the position is located behind the active Panel 3805. The deformation of the roof-to-floor convergence was more intense than that of the rib-to-rib convergence. The amount of roof-to-floor convergence was over 1.7 m at a distance of 150 m behind the active Panel 3805, whereas the rib-to-rib convergence was over 1.3 m at the same position. Roof collapse occurred in some sections, and severe floor heave occurred even though the floor was hardened. In addition, the rockbolts and anchor cables installed in the roof and rib were found to have become damaged.

Roof fissure distribution was carried out by using borehole imaging instrument (YTJ-20, Xuzhou City of China) behind the active Panel 3805 (see Fig. 3a). The first imaging fissure of the surrounding rock was conducted 45 m behind the active Panel 3805 while the second was 135 m behind the active Panel 3805. The imaging results were shown in Fig. 3b. The second imaging fissure of the surrounding rock failed to achieve due to the collapse of the borehole. It can be seen from Fig. 3b that the roof of the 3905 headgate was fractured in the 0–0.9 m depth range, the interface between the coal seam and the rock was at 1.4 m depth, and there was an obvious vertical crack more than 0.4 m long at 1.9 m depth.

3. Numerical simulation using finite element method based on FLAC3D

3.1. 3D numerical model configuration

Finite element method based on the FLAC3D software is widely used to simulate the behavior including the stress, deformation and plastic zone characteristics during retreating the longwall panel [30–38]. A global 3D numerical model was generated to simulate the failure mechanism of 3905 headgate (see Fig. 4). Panel 3805, Panel 3807, Panel 3905 and Panel 3907 were accounted for in this global 3D numerical model to simulate the mining-induced influence of the remnant pillar between panel 3805 and panel 3807 on the 3905 headgate surrounding rock stability. The modeling panel widths of Panel 3805, Panel 3807, Panel 3905 and Panel 3907 were 100 m, 100 m, 113.8 m and 86.2 m, respectively. The modeling cross sections of 3805 headgate and 3805 tailgate were 3.2 m high by 4.8 m wide. The modeling cross sections of 3905 headgate and 3905 tailgate were 3.6 m high by 4.8 m wide. Both of the barrier pillar widths in the coal seam 8# and coal seam 9# were 30 m. To evaluate the mining-induced influence and boundary effect, the length along the panel MD (y axial) was set to 320 m. Therefore, the dimension of the 3D global model is 239.6 m × 113 m × 320 m along the x, z, and y axial directions.

3.2. Mechanical properties of rock mass and coal seam and modeling process

The Mohr–Coulomb model was applied to simulate the rock mass and coal seams. According to the geological survey memoir,

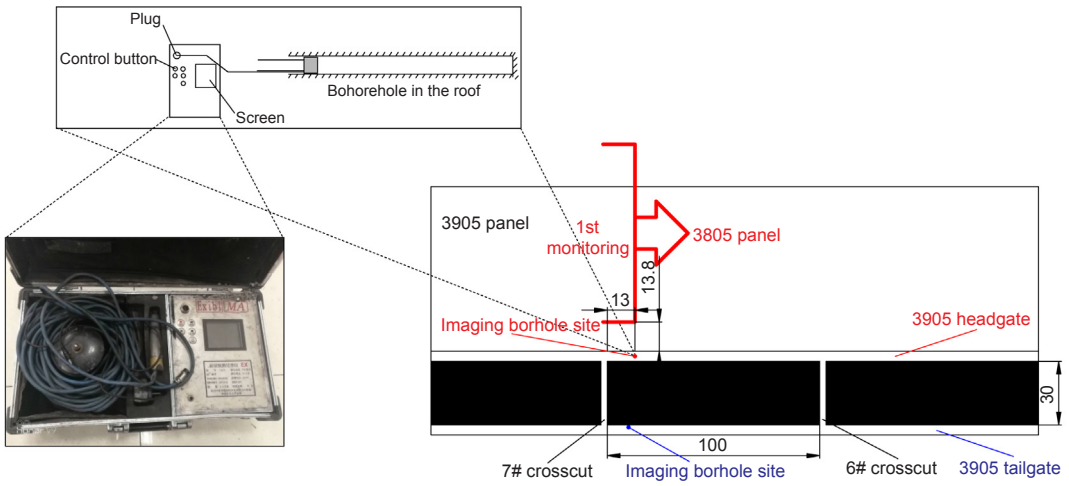

(a)

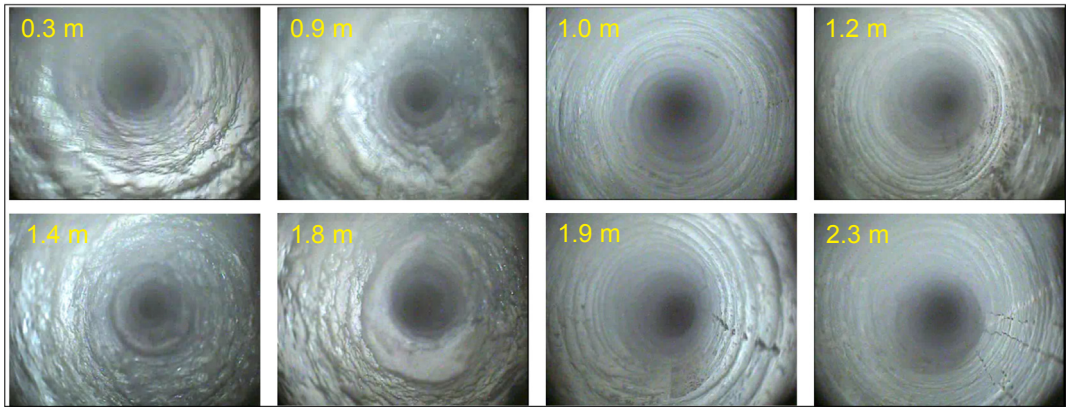

(b)

Fig. 3. Roof fissure distribution of surrounding rock in the 3905 headgate. (a) Borehole imaging instrument and site in the 3905 headgate (unit:m); (b) Imaging results at various distances to the borehole.

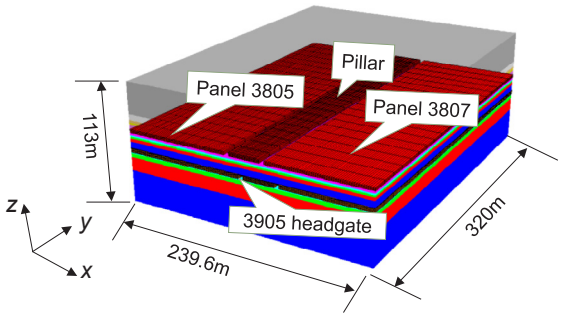

Fig. 4. Global 3D numerical model.

mechanical property parameters were provided by the Zhaiyadi Coal Mine through laboratory uniaxial compression tests [39]. Table 1 shows the mechanical properties of the rock mass and coal seams.

At the top of the 3D global model, the vertical stress (szz = 8.7275 MPa) is applied to simulate the overlying strata weight (cover depth 349.1 m). Both stress coefficients along the × and y axial directions are set to 1.0 according to a large number of in-situ ground stress test data [40–42]. The horizontal sides and bottom side are roller constrained. The modeling process is as follows: (i) calculating the initial stress state of the 3D global model; (ii) modeling the excavations of 3805 headgate and 3805 tailgate; (iii) retreating Panel 3807; (iv) modeling the excavations of 3905 headgate and 3905 tailgate, and retreating Panel 3805; (v) modeling with respect

Table 1
Rock strata properties used in the numerical model.

Rock strata	Thickness (m)	Bulk modulus (GPa)	Shear modulus (GPa)	Cohesion (MPa)	Friction angle (°)	Tensile strength (MPa)
Overlying strata	30	16.67	7.69	12.0	42	2.50
Sand mudstone	2.7	7.72	5.08	8.80	38	1.10
Fine sandstone	2.3	26.81	6.99	9.47	40	1.30
Gritstone	1.9	14.76	10.16	17.45	42	3.20
Limestone	4.6	22.62	11.05	27.68	46	5.80
Coal seam 8#	3.2	5.68	2.93	3.00	30	0.20
Mudstone	2.0	7.41	4.88	3.20	28	0.27
Fine sandstone	1.5	26.81	6.99	5.00	32	1.00
Sand mudstone	1.7	8.33	5.74	4.00	30	0.80
Fine sandstone	3.0	26.81	6.99	5.00	32	1.00
Mudstone	5.8	7.41	4.88	3.20	28	0.27
Coal seam 9#	4.5	5.68	2.93	3.0	25	0.15
Mudstone	0.7	7.41	4.88	1.60	14	0.05
Carbonaceous mudstone	3.7	6.67	4.00	1.80	16	0.10
Mudstone	12.7	7.41	4.88	2.50	22	0.39
Underlying strata	30	16.67	7.69	12.0	42	2.50

to the different roadway layout of coal seam 9#.

3.3. Calibration of the 3D global model

In order to calibrate the reliability of the 3D global model and the mechanical properties employed in the model, the calibrations of the 3D global model by comparing the outputs of the global model with in-situ observations are needed. Fig. 5 shows the comparison between the in-situ measured and simulated convergences of 3905 headgate during retreating panel 3805. The in-situ measured surrounding rock deformation curves are shown by triangles and squares while the simulated surrounding rock deformation is shown by the solid lines. Both the in-situ measured and numerical simulated surrounding rock deformation curves reveal similar characteristics. At the beginning (from 30 m ahead of the active panel 3805 to 20 m behind the active Panel 3805), both the roof to floor convergence and rib to rib convergence increase sharply. After some time (75 m behind of the active Panel 3805), both the roof to floor convergence and rib to rib convergence arrive a constant value.

Therefore, the numerical simulation stress–strain curve of the RBB matches in-situ measured surrounding rock deformation data very well. The calibrated input mechanical property parameters shown in Table 1 and the 3D global model can be applied to simulate 3905 headgate failure mechanism due to mining the upper coal seam.

4. Numerical simulation on the failure mechanism of 3905 headgate during retreating Panel 3805

4.1. Floor stress evolution after retreating Panel 3805

4.1.1. Floor stress with respect to the delay distance to the active Panel 3805

Floor stress varies with respect to the distance to the middle of the remnant pillar after retreating Panel 3805. Fig. 6 shows the stress distribution in the remnant pillar floor with respect to the delay distance to the active Panel 3805 (mining 140 m). The positive distance to the middle of the remnant coal pillar means that the position is located beneath the Gob 3807. Meanwhile, the negative distance to the middle of the remnant coal pillar means that the position is located beneath the Gob 3805. It can be seen that

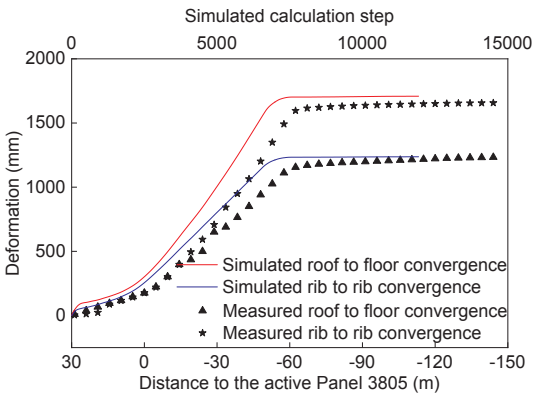

Fig. 5. Comparison between the in-situ measured and simulated convergences of 3905 headgate during retreating Panel 3805.

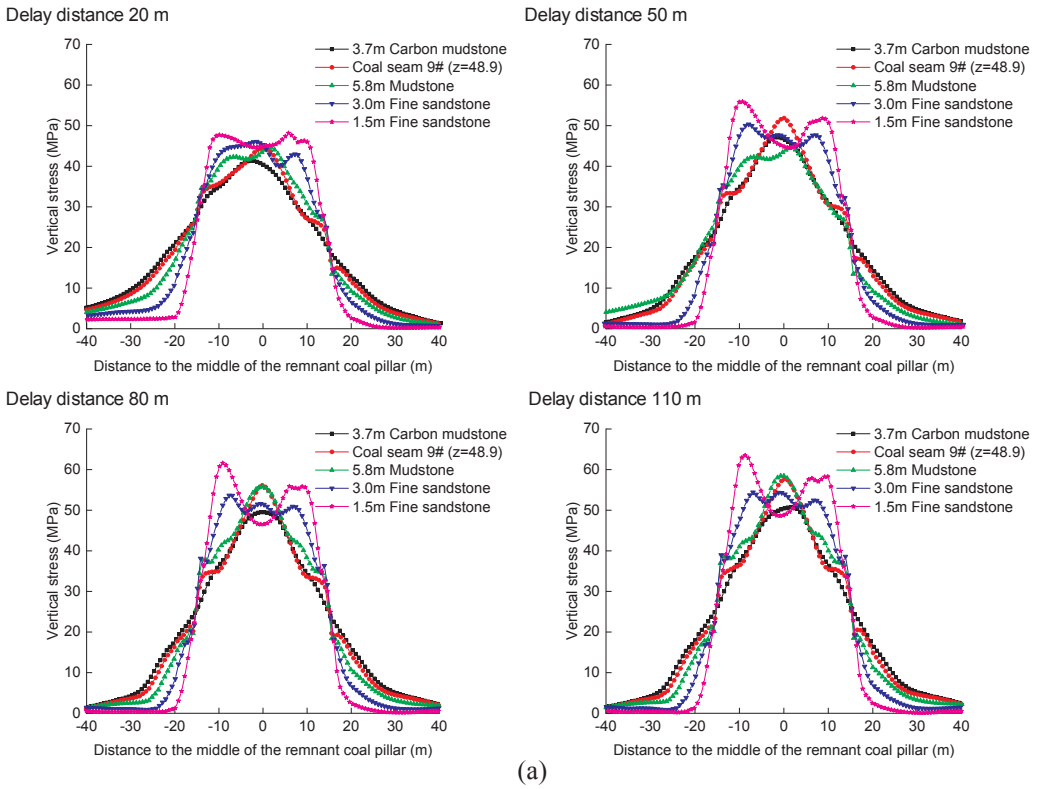

Fig. 6. stress distribution in the remnant pillar floor with respect to the delay distance to the active Panel 3805. (a) Vertical stress; (b) Horizontal stress.

(a) The peak floor vertical stress decreases as the vertical distance (VD) to the remnant coal pillar increases. Moreover, the peak floor vertical stress is with two peaks followed by one peak as the VD to the remnant coal pillar increases. The radius of the peak floor vertical stress decreases as the VD to the remnant coal pillar increases. When the delay distance to the active Panel 3805 is 20 m, the two peaks are located −9.5 m and 5.8 m away from the middle of the remnant coal pillar for the 1.5 m fine sandstone (2.75 m to the remnant coal pillar in the vertical direction); when the delay distance to the active Panel 3805 is 80 m, the two peaks are located −9.1 m and 8.9 m. No matter how many the delay distance to the active Panel 3805 is, the only one peak is located around the middle of the remnant coal pillar.

(b) The radius of the floor vertical stress concentration increases as the VD to the remnant coal pillar increases. When the delay distance to the active Panel 3805 is 20 m, the radius is located −18.0 m to 15.8 m away from the middle of the remnant coal pillar for the 1.5 m fine sandstone; when the delay distance to the active Panel 3805 is 80 m, the radius is located −17.0 m to 16.8 m away from the middle of the remnant coal pillar. Meanwhile, when the delay distance to the active Panel 3805 is 20 m, the radius is located −27.7 m to 20.0 m away from the middle of the remnant coal pillar for the coal seam 9# (16.7 m to the remnant coal pillar in the vertical direction); when the delay distance to the active Panel 3805 is 80 m, the radius is located −23.0 m to 23.3 m away from the middle of the remnant coal pillar. Thereby, the floor strata move a little from the Gob 3805 to the Gob 3807 as the delay distance to the active Panel 3805 increases. The floor strata shape horizontal dislocation in accordance with the horizontal stress distribution results.

(c) The peak floor horizontal stress increases as the VD to the remnant coal pillar increases. When the delay distance to the active Panel 3805 is less than 80 m, the peak floor horizontal stress is with only one peak. However, when the delay distance to the active Panel 3805 is more than 80 m, the peak floor horizontal stress is with two peaks followed by one peak as the VD to the remnant coal pillar increases. Under these conditions, the radius of the peak floor horizontal stress decreases as the VD to the remnant coal pillar increases. When the delay distance to the active Panel 3805 is 80 m, the two peaks are located −9.1 m and 8.9 m away from the middle of the remnant coal pillar for the 1.5 m fine sandstone, and the two peaks are located −7.4 m and 7.1 m away from the middle of the remnant coal pillar for the 3.0 m fine sandstone (6.7 m to the remnant coal pillar in the vertical direction).

(d) The radius of the floor horizontal stress concentration increases as the VD to the remnant coal pillar increases. When the delay distance to the active Panel 3805 is 20 m, the radius is located −17.6 m to 16.5 m away from the middle of the remnant coal pillar for the 1.5 m fine sandstone; when the delay distance to the active Panel 3805 is 80 m, the radius is located −17.3 m to 16.4 m away from the middle of the remnant coal pillar. Meanwhile, when the delay distance to the active Panel 3805 is 20 m, the radius is located −40.5 m to 26.1 m away from the middle of the remnant coal pillar for the coal seam 9#; when the delay distance to the active Panel 3805 is 80 m, the radius is located −27.2 m to 25.8 m away from the middle of the remnant coal pillar for the coal seam 9#.

4.1.2. Floor stress concentration factor (SCF) and stress transmission angle (STA) with respect to the delay distance to the active Panel 3805

Fig. 7 shows the floor SCF (x = 116.2, in the middle of 3905 headgate floor) after retreating Panel 3805. It can be seen that,

(a) The retreating of the Panel 3805 has a great influence on the floor vertical stress evolution, and that the influence range of floor vertical stress increment is about 40 m at front of the active Panel 3805 and 80 m behind the active Panel 3805. The floor vertical stress at front of the active Panel 3805 is less than that of behind the active Panel 3805 in accordance with the gob change of the upper coal seam. The floor vertical stress is stable in stage I, then increases rapidly in stage II, and then tends to be a constant

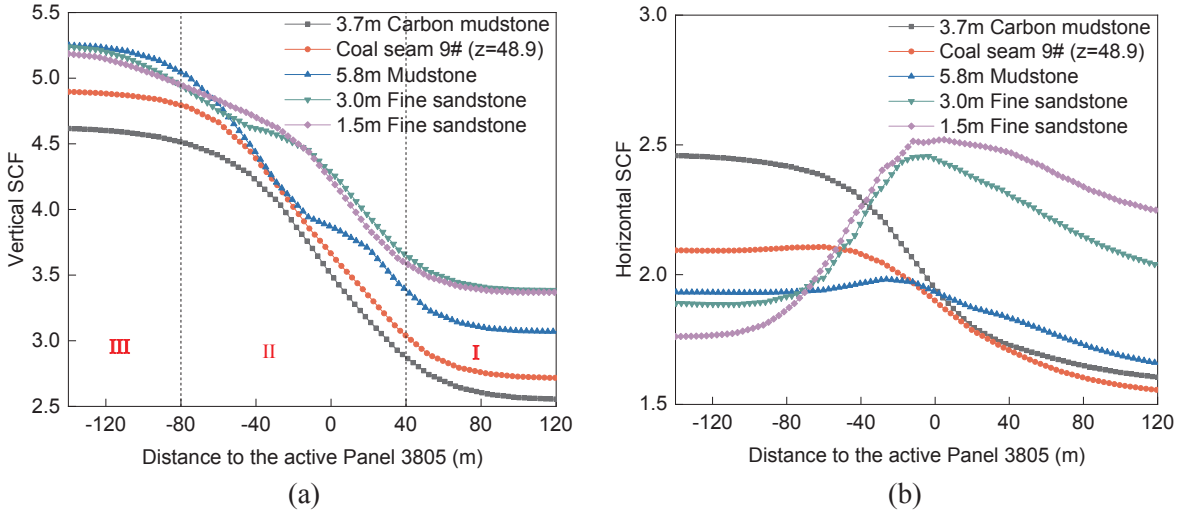

Fig.7. Floor stress concentration factor after retreating Panel 3805. (a) Vertical SCF; (b) Horizontal SCF.

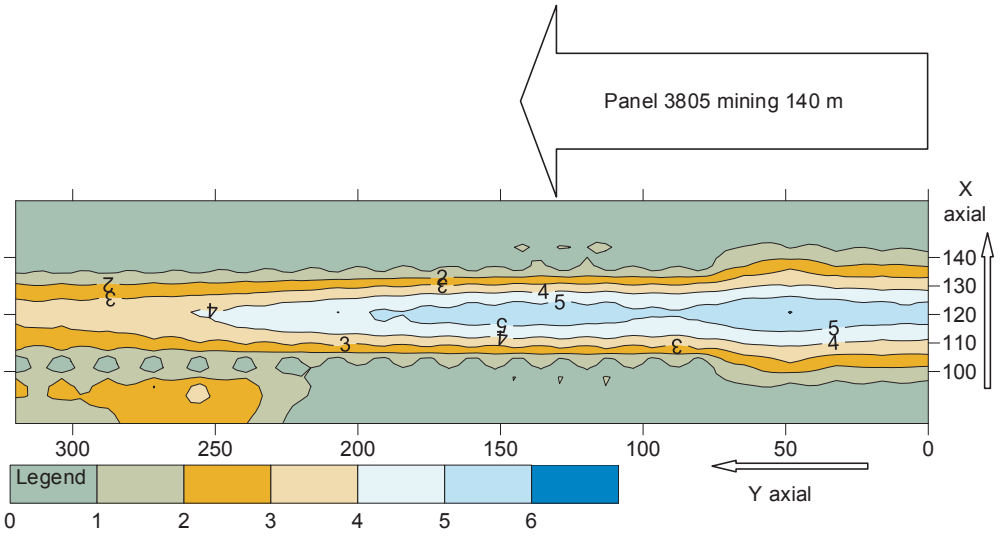

Fig. 8. SCF contour map in the coal seam 9# after retreating Panel 3805.

value in stage III. It can be seen that the peak vertical SCF in the coal seam 9# (the lower coal seam) is 4.9, located 100 m behind the active Panel 3805.

(b) The horizontal SCF presents a Λ-shape for the 1.5 m fine sandstone and 3.0 m fine sandstone, while the horizontal SCF of the farther floor strata increases and tends to be a constant value as the distance to the active Panel 3805 increases. The peak horizontal SCF decreases as the VD to the remnant coal pillar increases, while the peak point moves away from the active Panel 3805. It can be seen that the peak horizontal SCF in the coal seam 9# (the lower coal seam) is 2.1, located 30 m behind the active Panel 3805.

Fig. 8 shows the vertical SCF contour map in the coal seam 9#. It can be seen that the HD to the middle of the remnant coal pillar where the vertical stress is greater than in-situ stress varies with the distance to the active Panel 3805. The HD from 0 m to 75 m behind the active Panel 3805 is about 15–18.5 m, the HD from 75 m to 80 m behind the active Panel 3805 is about 18.5–25 m, and while the HD from 80 m to 140 m behind the active Panel 3805 is about 25 m. The HD from 0 m to 90 m at front of the active Panel 3805 is about 15–18.5 m, while the HD from 75 m to 180 m at front of the active Panel 3805 is about 15 m. Furtherly, Fig. 9 shows the calculation sketch map of the STA, and the calculation formula is shown as follows,

$$\theta = \arctan\left(\frac{\mathrm{HD}-D/2}{\mathrm{IT}}\right) \tag{1}$$

where θ is the stress transmission angle; D is the width of remnant coal pillar; HD is the horizontal distance to the middle of remnant coal pillar; IT is the interburden thickness between the upper coal seam and the horizontal level shown in Fig. 9. Hence, Table 2 presents the STA with respect to the distance to the active Panel 3805. It can be seen that the STA increases as the delay distance to the active Panel 3805 increases. Particularly, the STA increases rapidly from 75 m to 80 m behind the active Panel 3805. The STA 80 m behind the active Panel 3805 reaches a constant value of 30.9°.

4.2. Stress and deformation evolution of 3905 headgate with respect to the delay distance to the active Panel 3805

The delay distance to the active Panel 3805 plays an important role in the stress and plastic zone evolution of 3905 headgate (see

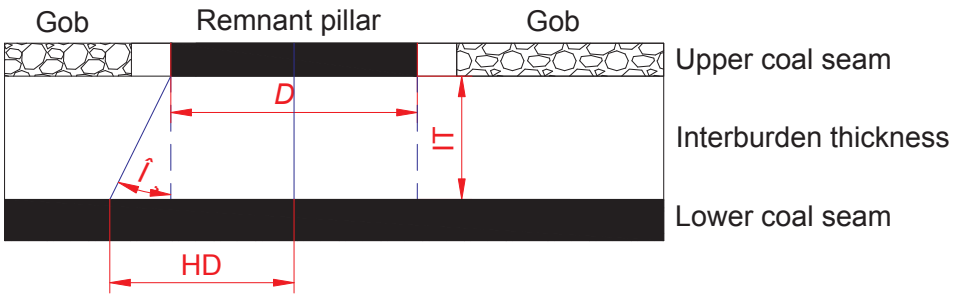

Fig. 9. Calculation sketch map of the stress transmission angle (STA).

Table 2
STA with respect to the distance to the active Panel 3805.

Distance to the active Panel 3805	STA (°)	Distance to the active Panel 3805	STA (°)
75 m to 180 m at front of the active Panel 3805	0	0 m to 75 m behind the active Panel 3805	0–11.8
0 m to 75 m at front of the active Panel 3805	0–11.8	75 m to 80 m behind the active Panel 3805	11.8–30.9
		80 m to 140 m behind the active Panel 3805	30.9

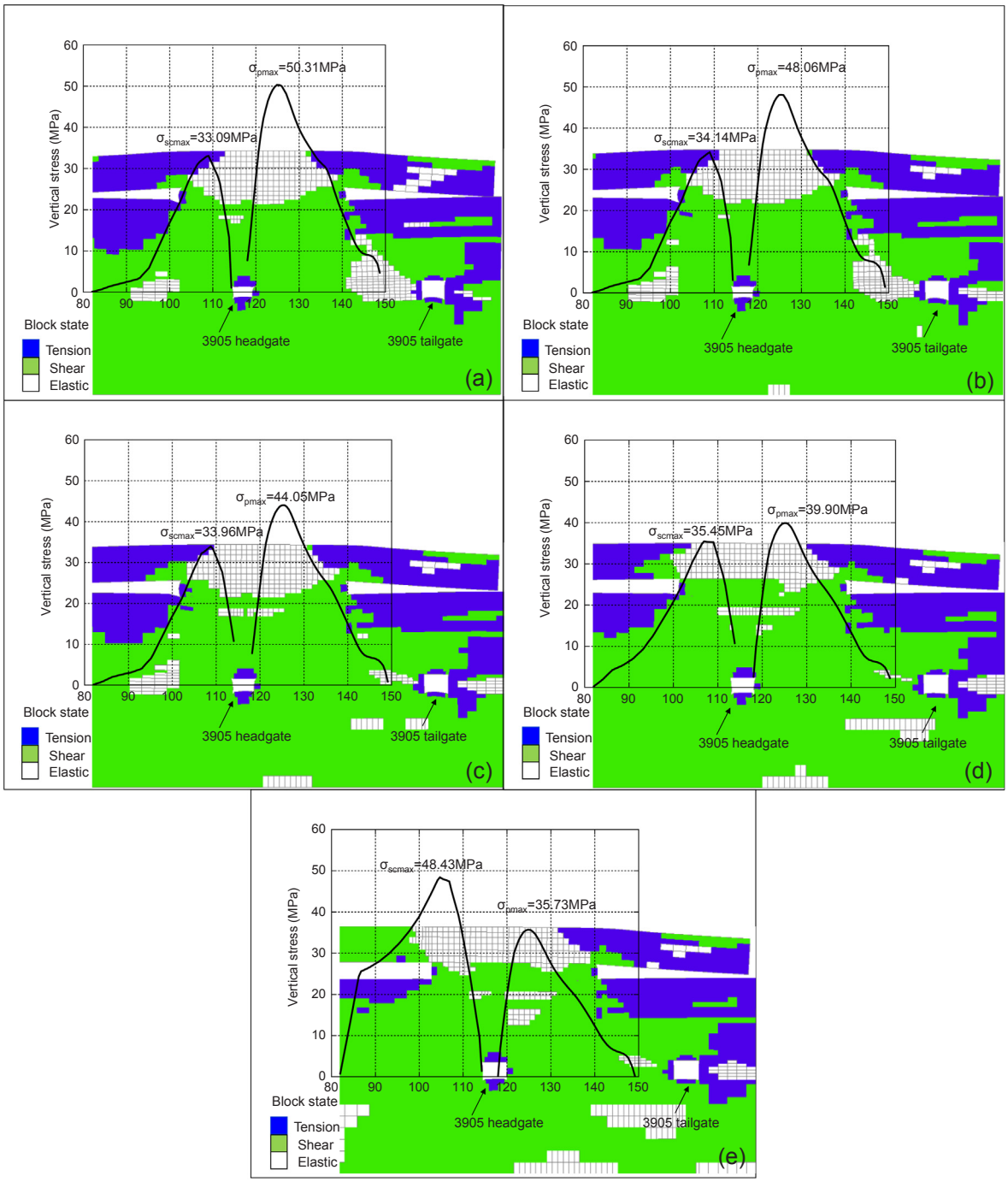

Fig. 10. Stress and plastic zone evolution of 3905 headgate with respect to the delay distance to the active Panel 3805. **(a)–(e)**: delay distance 124 m, 96 m, 64 m, 32 m, 0 m.

Table 3
Stress concentration factor of two ribs.

Delay distance to the active Panel 3805 (m)	Stress concentration factor of coal pillar rib	Stress concentration factor of solid coal rib	Ration of σ_{scmax} to σ_{pmax}
0	3.46	4.69	1.36
32	3.86	3.43	0.89
64	4.26	3.29	0.77
96	4.65	3.30	0.71
128	4.87	3.20	0.66

Fig. 10). It can be seen that

(a) Both the vertical stress in the middle of the coal pillar rib and the middle of the solid coal rib present a Λ-shaped distribution. The maximum vertical stress in the middle of the coal pillar rib (σ_{pmax}) increases as the delay distance to the active Panel 3805 increases while that of the solid coal rib (σ_{scmax}) tends to decrease. The initial vertical stress of the measured level is 10.33 MPa. The SCF of two ribs and the ratio of σ_{scmax} to σ_{pmax} are shown in Table 3. The results of the ratio of σ_{scmax} to σ_{pmax} indicate that the vertical stress transfers from the solid coal rib to the coal pillar rib.
(b) The peak point of σ_{scmax} moves away from the 3905 headgate as the delay distance to the active Panel 3805 increases. Meanwhile, the peak point of σ_{pmax} moves little. The detailed offset distance of the maximum vertical stress point to the middle of the 3905 headgate is shown in Table 4.
(c) The plastic zone area tends to increase as the delay distance to the active Panel 3805 increases, which is in strong accordance with the STA.

Fig. 11 shows the deformation of 3905 headgate with respect to the delay distance to the active Panel 3805. It can be seen that

(a) Surrounding rock deformation of the two ribs is characterized by disproportional distribution. The coal pillar rib deformation is more than the solid coal rib deformation. The ratio of coal pillar rib deformation to solid coal rib increases as the delay distance to the active Panel 3805 increases. The ratio reaches 1.37 as the delay distance to the active Panel 3805 is 96 m.
(b) Surrounding rock deformation of the roof and floor is also characterized by disproportional distribution. The roof subsidence is more than the floor heave. The ratio of roof subsidence to floor heave increases as the delay distance to the active Panel 3805 increases. The ratio reaches 1.12 as the delay distance to the active Panel 3805 is 96 m.
(c) No matter where the position behind the active Panel 3805 is, roof-to-floor convergence is more than rib-to-rib convergence. As the delay distance to the active Panel 3805 is 96 m, roof-to-floor convergence and rib-to-rib convergence reach 1546 mm and 1154 mm, respectively.

4.3. Discussion of 3905 headgate failure mechanism

As described in the in-situ observation and numerical simulation sections, the 3905 headgate failure mechanism can be preliminarily summarized as follows. 3905 headgate is located in a high stress condition due to the remnant pillar stress transfer of the upper coal seam. During retreating Panel 3805, the design of the lower coal seam entry (3905 headgate) and support strategies are unsuitable to maintain surrounding rock stability, especially as the delay distance to the active Panel 3805 increases. As well as the floor strata stress redistribution due to retreating the Panel 3805, the surrounding rock of 3905 headgate undergoes high vertical stress and horizontal stress and enters gradually into the plastic state. As the result of the concentrated vertical stress, obvious vertical fissuring occurred in the roof, the roof and floor of 3905 headgate undergo severe deformation. Meanwhile, the horizontal dislocation results in the rockbolt and cable failure of in the roof, and then the roof collapse occur suddenly. As the result of the concentrated vertical stress and horizontal stress, the solid coal rib and pillar rib undergoes severe deformation. Especially, the coal pillar rib deformation is more than the solid coal rib deformation due to the stress disproportional distribution. The stability of 3905 headgate is affected by the vertical stress and horizontal stress distribution of the surrounding rock due to retreating the Panel 3805. Based on these findings of the failure mechanism for 3905 headgate, an appropriate location of 3905 headgate will be discussed below, which will be helpful for entry surrounding rock stability.

Table 4
Offset distance of the maximum vertical stress point to the middle of the 3905 headgate (units: m).

Delay distance to the active Panel 3805	Offset distance of σ_{pmax}	Offset distance of σ_{scmax}
0	8.6	11.5
32	9.1	9.3
64	9.3	7.4
96	9.2	7.2
128	8.7	7.2

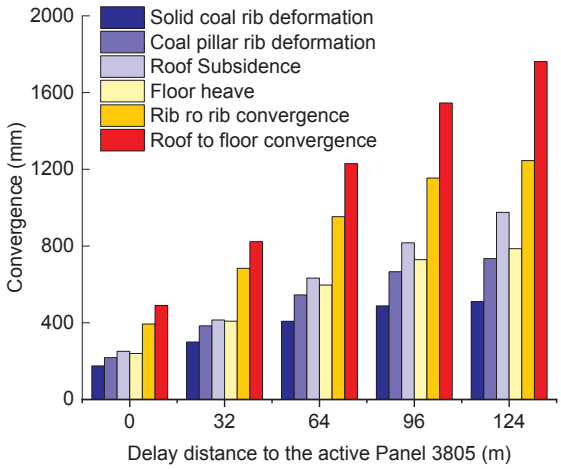

Fig. 11. Deformation of 3905 headgate with respect to the delay distance to the active Panel 3805.

5. Discussion

Based on above findings of the failure mechanism for 3905 headgate, the appropriate location of the lower coal seam entry are out of the stress concentration zone due to the remnant coal pillar of the upper coal seam. In order to determine an appropriate location of 3905 headgate, four numerical simulation schemes were carried out (see Fig. 12). Fig. 13 shows the stress and plastic zone evolution of 3905 headgate at the same delay distance to the active Panel 3805 (128 m). It can be seen that both the vertical stress in the middle of the coal pillar rib and the middle of the solid coal rib present a Λ-shaped distribution. The maximum vertical stress in the solid coal rib (σ_{scmax}) decreases sharply as the designed 3905 headgate moves away from the middle of the remnant coal pillar. Moreover, the maximum vertical stress in the solid coal rib (σ_{scmax}) is less than the in-situ stress where the 3905 headgate is located under the Gob 3805. The peak point of σ_{scmax} moves away from the 3905 headgate as the designed 3905 headgate moves away from the middle of the remnant coal pillar. Meanwhile, the peak point of σ_{pmax} moves little. The plastic zone area tends to increase as the designed 3905 headgate moves away from the middle of the remnant coal pillar.

Fig. 14 shows the deformation of 3905 headgate at the same delay distance to the active Panel 3805 (128 m). It can be seen that the coal pillar rib deformation is more than the solid coal rib deformation, and the floor heave is more than the roof subsidence. When the 3905 headgate is located under the Gob 3805, solid coal rib deformation, coal pillar rib deformation and floor heave change little. Meanwhile, the roof subsidence reaches a minimum value where the 3905 headgate is located 25 m away from the middle of the remnant coal pillar. The rib-to-rib convergence and roof-to-floor convergence would change little when the 3905 headgate is located 20 m to 30 m away from the middle of the remnant coal pillar. Moreover, the radius of the floor horizontal stress concentration in the coal seam 9# is about 25 m. In summary, the designed 3905 headgate located 25 m to 30 m away from the middle of the remnant coal pillar would be an alternative scheme.

In practice, the original 3905 headgate was abandoned due to severe deformation and the original 3905 tailgate (28.8 m away from the middle of the remnant coal pillar) after repair was modified as the new 3905 headgate. A new entry was excavated 30 m away from the original 3905 tailgate as the new 3905 tailgate. As a result, the rib-to-rib convergence of the new 3905 headgate reaches 212 mm and the floor heave of the new 3905 headgate reaches 32 mm, and the roof subsidence of the new 3905 headgate reaches 135 mm during the excavation stage. Moreover, the section of the new 3905 headgate meet the requirement of the mining of Panel 3905.

6. Conclusions

Some entries of the lower coal seam under the remnant coal pillar caused by extraction of the upper coal seam in the Zhaiyadi Coal Mine, which are subjected to high stress and large deformation, are difficult to maintain. Thus, the failure mechanism of the lower coal seam entry under the remnant pillar based on the in-situ observations and numerical simulations is urgent to reveal in Zhaiyadi Coal Mine.

A 3D numerical model is established to evaluate the stress, deformation and plastic zone evolution characteristics to find out the failure mechanism of 3905 headgate. In order to improve the reliability of the numerical simulations, the global model is validated by comparing the surrounding rock deformation of 3905 headgate with the in-situ observation data due to the extraction of Panel 3805. The results of the global model indicate that the peak floor vertical stress decreases, the radius of the floor vertical stress concentration, the peak floor horizontal stress and the radius of the floor horizontal stress concentration increase as the VD to the remnant coal pillar increases. When the delay distance to the active Panel 3805 is 80 m, the radius of the floor vertical stress concentration is located −23.0 m to 23.3 m away from the middle of the remnant coal pillar for the coal seam 9#, while the radius of the floor horizontal stress concentration is −27.2 m to 25.8 m. The floor strata shape horizontal dislocation in accordance with the

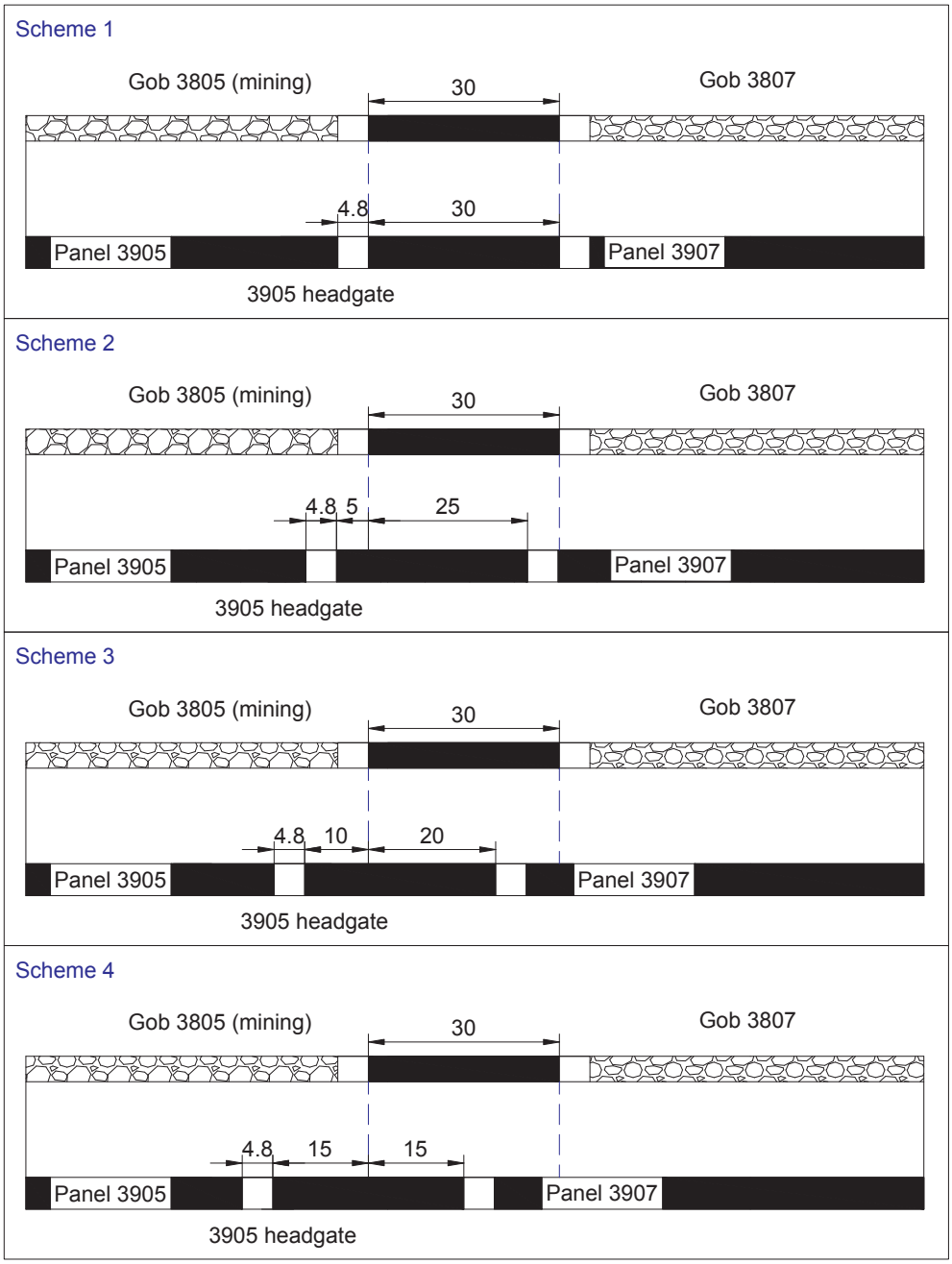

Fig. 12. Deformation of 3905 headgate with respect to the delay distance to the active Panel 3805 (units:m).

horizontal stress distribution results. The peak vertical SCF in the coal seam 9# (the lower coal seam) is 4.9, located 100 m behind the active Panel 3805 while the peak horizontal SCF in the coal seam 9# is 2.1, located 30 m behind the active Panel 3805. The STA 80 m behind the active Panel 3805 reaches a constant value of 30.9°.

After the 3905 headgate was excavated, the maximum vertical stress in the middle of the coal pillar rib (σ_{pmax}) increases as the delay distance to the active Panel 3805 increases while that of the solid coal rib (σ_{scmax}) tends to decrease. Both the ratio of coal pillar rib deformation to solid coal rib and the ratio of roof subsidence to floor heave increase as the delay distance to the active Panel 3805 increases. As the delay distance to the active Panel 3805 is 96 m, the ratios reach 1.37 and 1.12, respectively, and roof-to-floor convergence and rib-to-rib convergence reach 1546 mm and 1154 mm, respectively.

Numerical results based on different numerical schemes show that the designed 3905 headgate located 25–30 m away from the middle of the remnant coal pillar would located out of the floor horizontal stress concentration and vertical stress concentration in the coal seam 9#. Field test indicates that the newly designed 3905 headgate and 3905 tailgate could meet the requirement. This case

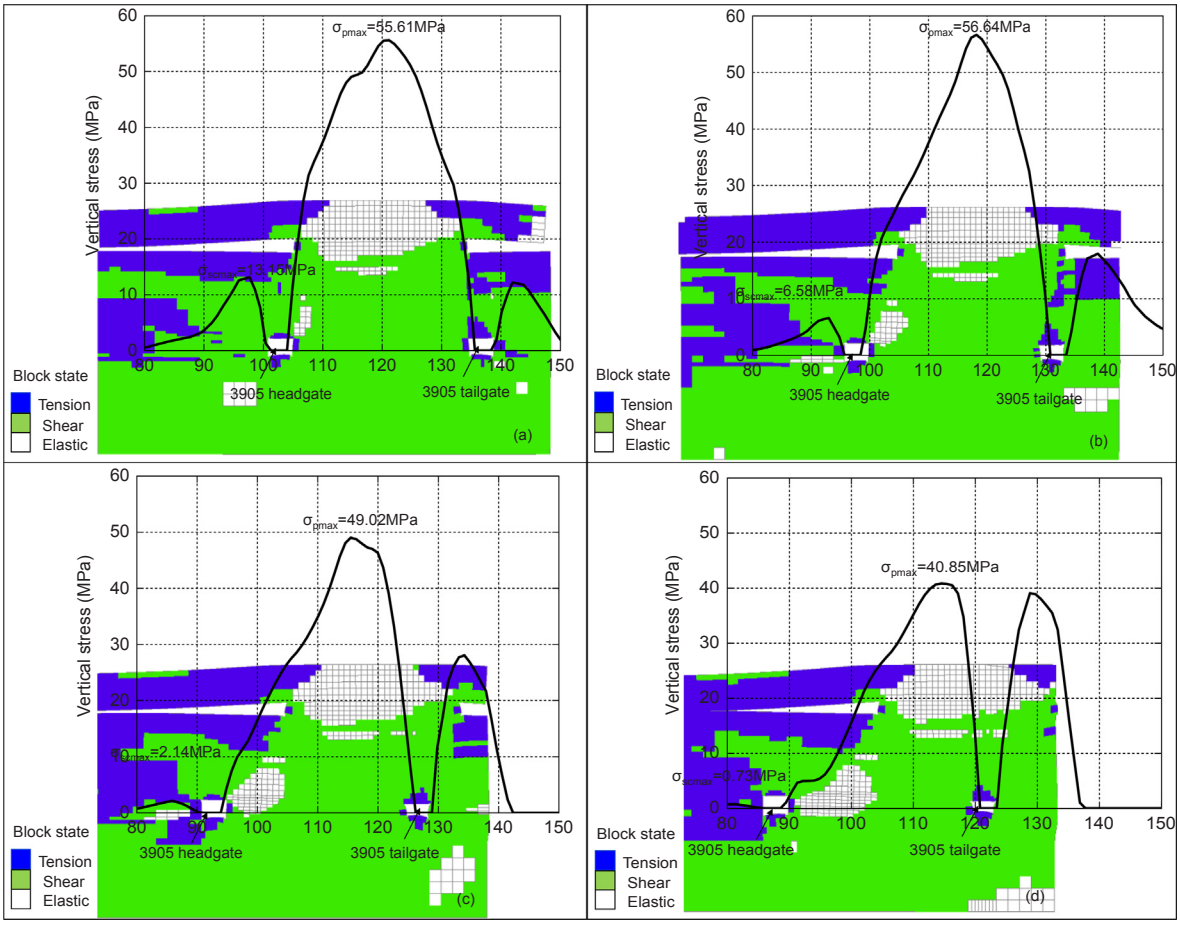

Fig. 13. Stress and plastic zone evolution of 3905 headgate with respect to the numerical scheme, **(a)–(d)**: scheme 1, scheme 2, scheme 3, scheme 4.

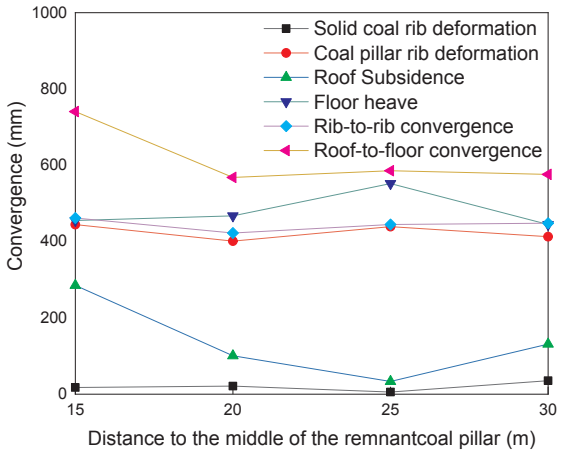

Fig. 14. Deformation of 3905 headgate with respect to the numerical scheme.

study will help with understanding the mining impacts of the upper coal seam and the remaining upper coal pillar upon the lower coal seam roadways, including under the coal pillar and the gob. The findings will help to provide a basis to select a reasonable location for lower coal seam roadways under similar mining and geological conditions.

Declaration of Competing Interest

The authors declare that they have no known competing financial interests or personal relationships that could have appeared to influence the work reported in this paper.

Acknowledgements

The authors acknowledge the financial support from the National Natural Science Foundation of China (No. 51804111, No.51974117), the Natural Science Foundation of Hunan Province (No. 2020JJ1141), and the Postgraduate Scientific Research Innovation Project of Hunan Province. The support of Zhaiyadi Coal Mine during in-situ observation is also acknowledged.

Appendix A. Supplementary material

Supplementary data to this article can be found online at https://doi.org/10.1016/j.engfailanal.2020.104638.

References

[1] T.B. Zhao, W.Y. Guo, Y.L. Tan, Y.C. Yin, L.S. Cai, J.F. Pan, Case studies of rock bursts under complicated geological conditions during multi-seam mining at a depth of 800 m, Rock Mech. Rock Eng. 51 (5) (2018) 1539–1564, https://doi.org/10.1007/s00603-018-1411-7.
[2] M. Christopher, E.C. Frank, M.P. Deno, Multiple-seam mining in the United States: design based on case histories, in: Proceedings of new technology for ground control in multiple-seam mining, Pittsburgh, PA, 2007, p. 15–27.
[3] Y.L. Tan, X.S. Liu, J.G. Ning, Y.W. Lv, In-situ investigations on failure evolution of overlying strata induced by mining multiple coal seams, Geotech. Test. J. 40 (2) (2017) 1–14, https://doi.org/10.1520/GTJ20160090.
[4] W.H. Sui, Y. Hang, L.X. Ma, Z.Y. Wu, Y.J. Zhou, G.Q. Long, L.B. Wei, Interactions of overburden failure zones due to multiple-seam mining using longwall caving, Bull. Eng. Geol. Environ. 74 (3) (2015) 1019–1035, https://doi.org/10.1007/s10064-014-0674-9.
[5] H. Guo, L. Yuan, B.T. Shen, Q.D. Qu, J.H. Xue, Mining-induced strata stress changes, fractures and gas flow dynamics in multi-seam longwall mining, Int. J. Rock Mech. Min. Sci. 54 (2012) 129–139, https://doi.org/10.1016/j.ijrmms.2012.05.023.
[6] J.G. Ning, J. Wang, Y.L. Tan, Q. Xu, Mechanical mechanism of overlying strata breaking and development of fractured zone during close-distance coal seam group mining, Int. J. Min. Sci. Technol. 30 (2) (2020) 207–215, https://doi.org/10.1016/j.ijmst.2019.03.001.
[7] F. Wang, J.L. Xu, J.L. Xie, Effects of arch structure in unconsolidated layers on fracture and failure of overlying strata, Int. J. Rock Mech. Min. Sci. 114 (2019) 141–152, https://doi.org/10.1016/j.ijrmms.2018.12.016.
[8] D.F. Zhu, S.H. Tu, Mechanisms of support failure induced by repeated mining under gobs created by two-seam room mining and prevention measures, Eng. Fail. Anal. 82 (2017) 161–178, https://doi.org/10.1016/j.engfailanal.2017.08.029.
[9] I.B. Tulu, T. Klemetti, G.S. Esterhuizen, J. Sumner, A case study of topography–related stress rotation effects on multi–seam stability, Proceedings of 33rd International Conference on Ground Control in Mining, Morgantown, 2014, pp. 1–7.
[10] A.M. Suchowerska, J.P. Carter, R.S. Merifield, Horizontal stress under supercritical longwall panels, Int. J. Rock Mech. Min. Sci. 70 (2014) 240–251, https://doi.org/10.1016/j.ijrmms.2014.03.009.
[11] W. Shen, L.M. Dou, H. He, G.A. Zhu, Rock burst assessment in multi-seam mining: a case study, Arabian J. Geosci. 10 (2017) 196, https://doi.org/10.1007/s12517-017-2979-z.
[12] X.Q. Fang, M.J. Guo, Z.Q. Lv, Instability mechanism and prevention of roadway under close-distance seam group mining, Chinese J. Rock Mech. Eng. 28 (10) (2009) 2059–2067, https://doi.org/10.3321/j.issn:1000-6915.2009.10.013.
[13] P.F. Jiang, H.P. Kang, J. Zhang, J. Lin, L.P. Si, Mechanism of load-transfer between coal pillars with different widths in mining the short-range seams, J. Min. Saf. Eng. 28 (3) (2011) 345–349, https://doi.org/10.3969/j.issn.1673-3363.2011.03.003.
[14] M.W. Zhang, H. Shimada, T. Sasaoka, K.K. Matsui, L.M. Dou, Evolution and effect of the stress concentration and rock failure in the deep multi-seam coal mining, Environ. Earth Sci. 72 (3) (2014) 629–643, https://doi.org/10.1007/s12665-013-2985-8.
[15] X.Q. Wei, H.B. Bai, H.R. Rong, Y. Jiao, B.Y. Zhang, Research on mining fracture of overburden in close distance multi-seam, Procedia Earth Planet. Sci. 2 (2011) 20–27, https://doi.org/10.1016/j.proeps.2011.09.004.
[16] C. Haycocks, M. Karmis, E. Barko, J. Carman, B. Ehgartner, S. Hudock, S. Webster, Ground control mechanisms in multi-seam mining, BuMine OFR 7–84 (1983) 328.
[17] S.S. Peng, U. Chandra, Getting the most from multiple-seam reserves, Coal Mining Process 17 (1980) 78–84.
[18] C. Haycocks, B. Ehgartner, M. Karmis, E. Topuz, Pillar load transfer mechanisms in multiple-seam mining, Soc. Min. Eng, AIME preprint, 1982, pp. 82–89.
[19] H. Yan, M.Y. Weng, R.M. Feng, W.K. Li, Layout and support design of a coal roadway in ultra-close multiple-seams, J. Central South Univ. 22 (11) (2015) 4385–4395, https://doi.org/10.1007/s11771-015-2987-7.
[20] Z.H. Liu, S. Lou, X.R. Meng, Z.N. Gao, Mining affect of close distance coal seam to surrounding rock stress evolution of coal face in distressed zone, J. Min. Saf. Eng. 33 (1) (2016) 102–108, https://doi.org/10.13545/j.cnki.jmse.2016.01.016.
[21] W. Yang, C.Y. Liu, Y. Yang, Reasonable malposition setting in close distance coal seams under influence of interlaminar stresses, Chinese J. Rock Mech. Eng. 31 (S1) (2012) 2965–2972, https://doi.org/10.3969/j.issn.1000-6915.2012.z1.049.
[22] X.R. Meng, C.H. Xu, Z.N. Gao, X.Q. Wang, Stress distribution and damage mechanism of mining floor, J. China Coal Soc. 35 (11) (2010) 1832–1836, https://doi.org/10.13225/j.cnki.jccs.2010.11.012.
[23] S.Y. Zhu, Z.Q. Jiang, P. Yao, W.G. Xiao, Application of analytic method in calculating floor stress of a working face, J. Min. Saf. Eng. 24 (2) (2007) 191–194, https://doi.org/10.3969/j.issn.1673-3363.2007.02.015.
[24] L.F. Wang, Z.C. Chang, Z.B. Yang, X.F. Wang, D.D. Qin, Combined support technology of roadway under mined gob of ultra-distance seams in deep mine, J. Min. Saf. Eng. 35 (4) (2018) 686–692, https://doi.org/10.13545/j.cnki.jmse.2018.04.004.
[25] X.J. Liu, X.M. Li, W.D. Pan, Analysis on the floor stress distribution and roadway position in the close distance coal seams, Arabian J. Geosci. 9 (2016) 83, https://doi.org/10.1007/s12517-015-2035-9.
[26] T.Q. Xiao, J.B. Bai, L. Xu, X.B. Zhang, Characteristics of stress distribution in floor strata and control of roadway stability under coal pillars, Min. Sci. Technol. (China) 21 (2) (2011) 243–247, https://doi.org/10.1016/j.mstc.2011.02.016.
[27] W. Zhang, D.S. Zhang, D.H. Qi, W.M. Hu, Z.M. He, W.S. Zhang, Floor failure depth of upper coal seam during close coal seams mining and its novel detection method, Energy Explor. Exploit. 36 (5) (2018) 1265–1278, https://doi.org/10.1177/0144598717747622.
[28] D.Z. Kong, Z.H. Wang, Z.C. Ren, Determining the optimum position of roadways of full-mechanized caving face in the close distance seams, J. Min. Saf. Eng. 31 (2) (2014) 270–276, https://doi.org/10.13545/j.issn1673-3363.2014.02.017.
[29] A.M. Suchowerska, R.S. Merifield, J.P. Carter, Vertical stress changes in multi-seam mining under supercritical longwall panels, Int. J. Rock Mech. Min. Sci. 61 (2013) 306–320, https://doi.org/10.1016/j.ijrmms.2013.02.009.
[30] Z.Z. Zhang, X.Y. Yu, H. Wu, M. Deng, Stability control for gob-side entry retaining with supercritical retained entry width in thick coal seam longwall mining,

Energies 12 (7) (2019) 1375, https://doi.org/10.3390/en12071375.
[31] Z.Z. Zhang, W.J. Wang, S.Q. Li, J.B. Bai, S.P. Hao, H. Wu, X.Y. Yu, An innovative approach for gob-side entry retaining with thick and hard roof: a case study, Technical Gazette 25 (4) (2018) 1028–1036, https://doi.org/10.17559/TV-20160816155022.
[32] L.S. Jiang, P. Kong, J. Shu, K.G. Fan, Numerical analysis of support designs based on a case study of a longwall entry, Rock Mech. Rock Eng. 52 (2019) 3373–3384, https://doi.org/10.1007/s00603-018-1728-2.
[33] G.C. Zhang, Z.J. Wen, S.J. Liang, Y.L. Tan, L. Tian, Y.Q. Zhao, D.S. Zhao, Ground response of a gob-side entry in a longwall panel extracting 17 m-thick coal seam: a case study, Rock Mech. Rock Eng. 53 (2020) 497–516, https://doi.org/10.1007/s00603-019-01922-5.
[34] W.F. Li, J.B. Bai, S.S. Peng, X.Y. Wang, Y. Xu, Numerical modeling for yield pillar design: a case study, Rock Mech. Rock Eng. 48 (2014) 305–318, https://doi.org/10.1007/s00603-013-0539-8.
[35] J. Wang, P.Q. Qiu, J.G. Ning, L. Zhuang, S. Yang, A numerical study of the mining-induced energy redistribution in a coal seam adjacent to an extracted coal panel during longwall face mining: a case study, Energy Sci. Eng. 8 (3) (2020) 817–835, https://doi.org/10.1002/ese3.553.
[36] C. John, F.Q. Gao, S. Doug, E. Davide, Numerical modelling of the effects of weak immediate roof lithology on coal mine roadway stability, Int. J. Coal Geol. 90–91 (2012) 100–109, https://doi.org/10.1016/j.coal.2011.11.003.
[37] Q.S. Bai, S.H. Tu, F.T. Wang, C. Zhang, Field and numerical investigations of gateroad system failure induced by hard roofs in a longwall top coal caving face, Int. J. Coal Geol. 173 (2017) 176–199, https://doi.org/10.1016/j.coal.2017.02.015.
[38] G.C. Zhang, L.J. Chen, Z.J. Wen, M. Chen, G.Z. Tao, Y. Li, H. Zuo, Squeezing failure behavior of roof-coal masses in a gob-side entry driven under unstable overlying strata, Energy Sci. Eng. (2020), https://doi.org/10.1002/ese3.678.
[39] Z.Z. Zhang, M. Deng, J.B. Bai, X.Y. Yu, Q.H. Wu, L.S. Jiang, Strain energy evolution and conversion under triaxial unloading confining pressure tests due to gob-side entry retained, Int. J. Rock Mech. Min. Sci. 126 (2020) 104184, , https://doi.org/10.1016/j.ijrmms.2019.104184.
[40] H.P. Kang, B.D. Yi, F.Q. Gao, H.W. Lv, Database and characteristics of underground in-situ stress distribution in Chinese coal mines, J. China Coal Soc. 44 (1) (2019) 23–33, https://doi.org/10.13225/j.cnki.jccs.2018.5032.
[41] H.P. Kang, L.P. Si, X. Zhang, Characteristics of underground in-situ stress distribution in shallow coal mines and its applications, J. China Coal Soc. 41 (6) (2016) 1332–1340, https://doi.org/10.13225/j.cnki.jccs.2016.0541.
[42] H.P. Kang, J. Lin, L.X. Yan, X. Zhang, Y.Z. Wu, L.P. Si, Study on characteristics of underground in-situ stress distribution in Shanxi coal mining fields, Chin. J. Geophys. 52 (7) (2009) 1782–1792, https://doi.org/10.3969/j.issn.0001-5733.2009.07.012.